

Influence of Octahedral Ligand Field Distortions and Temperature on the Electrochromic Response of Tungsten Oxides

Matthew Chagnot,¹ Noah P. Holzapfel,¹ Loukas Kollias,² Yue Yu,³ Giannis Mpourmpakis,^{2,4} and
Veronica Augustyn^{1,*}

¹ Department of Materials Science and Engineering, North Carolina State University, Raleigh,
NC 27695, United States

² School of Chemical Engineering, National Technical University of Athens (NTUA), Athens, GR-
15780, Greece

³ Department of Applied and Engineering Physics, Cornell University, Ithaca, NY 14853, United
States

⁴ Department of Chemical and Petroleum Engineering, University of Pittsburgh, Pittsburgh,
Pennsylvania 15261, United States

* corresponding author email: vaugust@ncsu.edu

Abstract

Tungsten oxides are electrochromic materials whose reversible color change in response to an applied voltage renders them useful for smart windows, adaptive displays, and color-changing wearables. The atomic structure, composition, and microstructure of tungsten oxides influences the resulting optical and electrochemical properties. At the atomic level, electrochromism is governed by the local structure of tungsten metal centers. Subtle structural distortions, such as octahedral tilts, bond length asymmetries, and ligand identity changes can induce shifts in d-orbital splitting energies. These can have significant impact on redox behavior and optical transitions. Temperature further influences the electrochromic response by affecting ion mobility, interfacial stability, and reaction pathways during electrochemical cycling. In this work, we characterized the electrochromic properties of crystalline tungsten oxide thin films in acidic aqueous electrolytes, establishing how structural distortions facilitate dual band electrochromism in $\text{WO}_3 \cdot 2\text{H}_2\text{O}$, a desirable property for independently modulating visible and infrared light. We also demonstrate that lower operating temperatures enhance coloration efficiency by suppressing parasitic hydrogen evolution, improving both switching contrast and cycling stability in aqueous environments.

1. Introduction

Electrochromism is the reversible modulation of a material's optical properties in response to an applied electrical voltage in the presence of an electrolyte. Electrochromic materials find broad utility in technologies such as energy-saving smart windows, anti-glare rearview mirrors, adaptive displays, and responsive wearable devices.^{1–3} The growing demand for tunable optical components has driven extensive research into both the discovery of new materials and a deeper mechanistic understanding of established materials to enable precise control over electrochromic behavior. Among the electrochromic materials explored to date, tungsten oxide (WO_3) stands out due to its pronounced color change—from transparent to deep blue—upon cathodic polarization.⁴ This coloration is associated with the reversible formation of tungsten bronzes, A_xWO_3 , where A represents an intercalated cation such as H^+ , Li^+ , or Na^+ .⁵

Cation-insertion coupled electron transfer into the WO_3 framework to form A_xWO_3 modifies its electronic structure and optical absorption characteristics. Fundamentally, this behavior stems from the electronic band structure of WO_3 : the valence band is dominated by fully occupied O 2p states, while the conduction band comprises empty W 5d orbitals, yielding a semiconductor with a band gap of approximately 3.0–3.3 eV in its bleached (transparent) state.⁶ Electron transfer leads to partial reduction of W^{6+} and population of the conduction band or localized states in the band gap, contributing to light absorption in the “colored” state.⁷ At the atomic level, electrochromism in WO_3 is determined by the local structure of tungsten metal centers. Subtle structural distortions, such as octahedral tilts, bond length asymmetries, and ligand identity changes can induce shifts in d-orbital splitting energies and thus electrochromic behavior. This connection opens opportunities to tailor electrochromic performance through precise structural modifications.

One such structural modification involves the incorporation of structural water into the tungsten oxide lattice, yielding crystalline and amorphous hydrates, $\text{WO}_3 \cdot n\text{H}_2\text{O}$.^{8–10} These hydrated oxides adopt distinct crystal structures and possess different ion transport properties

relative to anhydrous WO_3 . Early investigations into hydrous tungsten oxides noted enhanced optical switching speeds, attributed to faster solid state ion transport in the hydrous polymorphs.⁸ Building on these findings, our previous work¹⁰ explored how structural water impacts not just the inserted ion mobility but the nature of optical modulation. We compared the electrochromic behavior of crystalline $\gamma\text{-WO}_3$ and orthorhombic $\text{WO}_3\cdot\text{H}_2\text{O}$ in a non-aqueous Li^+ electrolyte. Our studies revealed that the hydrate exhibited dual-band electrochromism, where initial polarization led to decreased optical transmission in the near-infrared (NIR) spectrum followed by visible light attenuation at higher states of charge. In contrast, $\gamma\text{-WO}_3$ displayed simultaneous changes in both spectral regimes across all states of charge. We hypothesized that the open framework of $\text{WO}_3\cdot\text{H}_2\text{O}$ supports an extended solid-solution insertion region, in contrast to the more constrained γ -phase. This further led us to hypothesize that solid solution insertion would facilitate electrochromic performance at low temperatures. However, the influence of structural water on the electronic structure remained unresolved, as did the influence of the temperature.

The present study aims to bridge that gap by investigating the effects of structural water and temperature on the electrochromic response of crystalline tungsten oxides, this time focusing on protons as the charge-compensating electrolyte species. We conducted operando UV/Vis/NIR spectroelectrochemical experiments on thin films of $\gamma\text{-WO}_3$ and monoclinic $\text{WO}_3\cdot 2\text{H}_2\text{O}$ in aqueous inorganic acidic electrolytes between -20°C to 20°C . We performed complementary density functional theory (DFT) calculations to elucidate the electronic density of states (DOS) and provide atomic-level insight into structure–optical property relationships. Our results reveal that the distinct electrochromic behaviors of $\gamma\text{-WO}_3$ and monoclinic $\text{WO}_3\cdot 2\text{H}_2\text{O}$ stem from differences in the local coordination environment of tungsten induced by the presence of structural water. We further find that in strong acid electrolytes, the electrochromic response improves at low temperatures due to decreased influence of the parasitic hydrogen evolution reaction (HER). These findings deepen the mechanistic understanding of electrochromism in tungsten oxides and

highlight strategies to fine-tune the electrochromic properties of transition metal oxides through rational control of the crystal structure and transition metal coordination.

2. Methods

Chemicals: All chemicals were used as received. Sodium tungstate dihydrate ($\text{Na}_2\text{WO}_4 \cdot 2\text{H}_2\text{O}$; 99+%), platinum wire (0.5 mm diameter, 99.99% trace metals basis), and FTO-coated glass (2.2 mm thickness, $7 \Omega/\text{sq}$) were purchased from Millipore Sigma. Concentrated sulfuric acid (H_2SO_4 ; 95.0 – 98.0%, ACS Grade), potassium hydroxide (KOH, Certified ACS), and ammonium hydroxide (NH_4OH , Certified ACS Plus) were purchased from Fisher Scientific. Argon gas (industrial grade) was purchased from Arc3 Gases. Hydrogen peroxide (30% by weight in H_2O , ACS) was purchased from Macron Fine Chemicals.

Electrodeposition: $\text{WO}_3 \cdot 2\text{H}_2\text{O}$ thin films were prepared by electrochemical deposition onto cleaned fluorinated tin oxide (FTO)-coated glass via a previously reported method.¹¹ Briefly, the deposition solution was prepared by heating 25 mL of a 12 mM aqueous solution of $\text{Na}_2\text{WO}_4 \cdot 2\text{H}_2\text{O}$ in deionized (DI) water to 75°C. 687 μL of concentrated H_2SO_4 was added to the heated $\text{Na}_2\text{WO}_4 \cdot 2\text{H}_2\text{O}$ solution while stirring to obtain a solution with a concentration of 0.5 M H_2SO_4 . The electrodeposition solution was placed in a 50 mL glass three-neck-flask (Kontes). The working electrode was 0.5 x 3 cm FTO-coated glass, the counter electrode was platinum wire, and the reference electrode was Ag/AgCl in saturated KCl (Pine Instruments). Films were electrodeposited onto a 1 cm^2 geometric area of the working electrode via cyclic voltammetry between -0.2 and 1 V vs. Ag/AgCl at 100 mV/s for 3 hours (450 cycles). After electrodeposition, the working electrode was immersed in 0.5 M H_2SO_4 overnight to promote film crystallinity. Anhydrous WO_3 films were prepared by heating the as-electrodeposited $\text{WO}_3 \cdot 2\text{H}_2\text{O}$ films at 350°C in air for 12 hours. FTO-coated glass was cleaned by sonicating for 10 minutes in soapy water,

acetone, ethanol, 1 M KOH, deionized (DI) water, and a basic piranha solution consisting of NH_4OH , 30% hydrogen peroxide, and DI water, respectively.

Physical Characterization: Room-temperature Raman spectra were collected using a Witec Alpha300r confocal microscope. Spectra were acquired using a 532 nm Nd:YAG laser at 100x magnification (Zeiss), averaged over 7 scans of 8 seconds each. Cryo-electron microscopy (cryo-EM) was performed on an FEI/Thermo Fisher Titan Themis cryoS/TEM microscope operated at 300 kV with a Gatan 626 cryo-transfer holder. Measurements were acquired at liquid nitrogen temperatures, and the sample temperature was estimated as the sample holder temperature, measured by a Gatan model 1905 temperature controller. In situ heating to 25 °C was performed with the same temperature controller and images were acquired after the temperature stabilized.

UV/VIS Spectroelectrochemical Measurements: Temperature-dependent UV/VIS spectroelectrochemistry was obtained using an Ocean HDX spectrometer (OceanOptics) equipped with a tungsten halogen light source (OceanOptics HL-2000) and a Qpod 3e temperature-controlled cuvette holder (Quantum Northwest). Spectra were collected using 0.1 second acquisition time, averaged over 10 spectra. Temperatures down to -20°C were achieved by cooling the temperature-controlled cuvette holder with a constant flow of ice-water and Ar gas (to prevent condensation). The electrochemical cell consisted of a quartz cuvette (Perkin Elmer 10 mm path length) containing $\text{WO}_3 \cdot 2\text{H}_2\text{O}$ or WO_3 on FTO-coated glass as the working electrode, Pt wire as the counter electrode, and a leakless Ag/AgCl in saturated KCl reference electrode. A custom-made cuvette cap was 3D-printed using a polylactic acid filament to hold the electrodes in place within the cuvette. The electrolyte was 3 mL of 5 M H_2SO_4 . Cyclic voltammetry (CV) was performed with a BioLogic MPG-2 potentiostat at scan rates between 1 and 100 mV/s.

DFT calculations: The density of states (DOS) was calculated with spin-polarized density functional theory (DFT) calculations, which were performed using the CP2K software package.¹² Unit cells were optimized using the Perdew-Burke-Ernzerhof functional with Grimme's 3rd order dispersion corrections (PBE-D3). PBE-D3 is known to accurately predict lattice parameters.^{13,14}

Subsequently, the Heyd-Scuseria-Ernzerhof (HSE06)^{15–17} range-separated hybrid exchange – correlation functional was used to calculate the DOS on the PBE-D3-optimized cells. Hybrid functionals are known to improve the accuracy of the calculated DOS when compared with commonly used generalized gradient approximation (GGA) functionals.^{18,19} Goedecker, Teter, and Hutter pseudopotentials were used to approximate the effect of core electrons.^{20,21} Double- ζ valence plus polarization (DZVP) basis sets were used for W, and triple- ζ (TZVP) for H, O atoms. A 600 Ry kinetic energy cutoff was applied for plane-wave expansion as implemented in the mixed Gaussian and plane-waves method in CP2K.²² The HSE06 calculated DOS was constructed using the auxiliary density matrix method.²³ The cFIT10 auxiliary basis set was used for W, while cFIT3 was used for H, O. DOS were shifted by the Fermi level, E_F , that corresponds to the energy of the highest occupied molecular orbital (HOMO) in our calculations. The degree of protonation, x , is equal to 0.5 for the protonated systems in the DFT calculations.

Additional information on the computational procedures (**Section 1-3** and **Figures S1-S7**), physical and electrochemical characterization of the materials (**Section 4**, **Figures S8-S11**) and electrochemical kinetic analysis (**Section 5**, **Figure S12**, **Table S4**) can be found in the Supplementary Information, SI.^{24–31}

3. Results and Discussion

We investigated the temperature-dependent UV-VIS spectroelectrochemistry of tungsten oxides using electrodeposited thin films of $\text{WO}_3 \cdot 2\text{H}_2\text{O}$ and WO_3 . We used Raman spectroscopy (**Figure S8**), SEM (**Figure S9**)²⁵, and cryo-TEM (**Figure 1**) to determine the crystal structure and microstructure of the deposited films. Raman spectroscopy shows that electrodeposition led to monoclinic $\text{WO}_3 \cdot 2\text{H}_2\text{O}$ thin films while SEM images show that they consist of platelet-like nanoparticles. Annealing the films at 350°C in air led to the formation of $\gamma\text{-WO}_3$ with a similar microstructure. We performed cryo-TEM to study the dehydration mechanism of a single $\text{WO}_3 \cdot 2\text{H}_2\text{O}$ platelet (synthesized via a precipitation reaction³²) and determine whether it influenced the microstructure. This is important because the electrochromic response is sensitive to the particle size and shape.^{33,34} Dehydration took place via in situ heating from -195°C to 25°C under vacuum (10^{-8} Torr). **Figure 1** shows that the dehydration of a platelet of monoclinic $\text{WO}_3 \cdot 2\text{H}_2\text{O}$ to $\gamma\text{-WO}_3$ occurs with no change in the platelet shape, although the overall thickness decreased from 208 Å to 169 Å. This is expected given that the interplanar spacing of the $\text{WO}_3 \cdot 2\text{H}_2\text{O}$ (010) is 6.9 Å and removal of the interlayer water should lead to a higher density crystal structure. As a result, in line with the SEM images in **Figure S9**²⁵, dehydration of $\text{WO}_3 \cdot 2\text{H}_2\text{O}$ leads to minimal microstructural changes and we can associate differences in the electrochromic response with differences in their crystal structure.

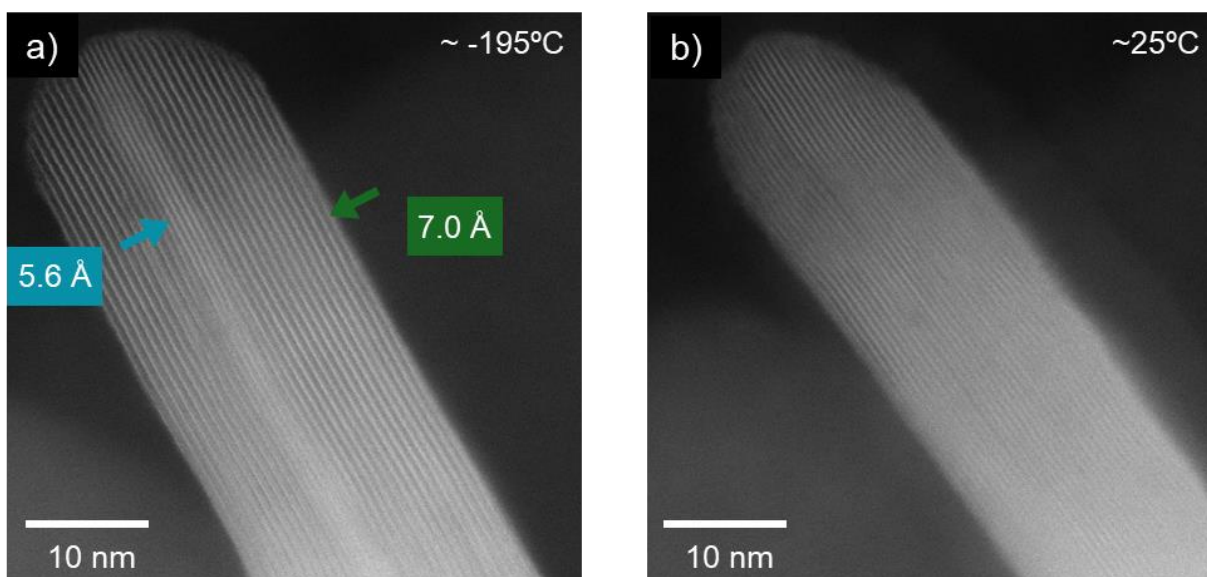


Figure 1. Cryo-transmission electron micrographs of a $\text{WO}_3 \cdot 2\text{H}_2\text{O}$ platelet subjected to in-situ heating from -195°C to 25°C under vacuum. At -195°C (a) the platelet is predominantly monoclinic $\text{WO}_3 \cdot 2\text{H}_2\text{O}$ as shown by the presence of crystal planes with an interlayer spacing of $\sim 6.9 \text{ \AA}$. Partial dehydration of the platelet under vacuum was observed as indicated by some collapsed layers with a decreased interlayer spacing of $\sim 5.6 \text{ \AA}$. After heating to 25°C (b), the structure of the entire platelet is consistent with $\gamma\text{-WO}_3$ (lattice spacing $\sim 5.5 \text{ \AA}$), indicating successful complete dehydration.

We performed operando UV/Vis/NIR spectroelectrochemistry during cyclic voltammetry in a strong acid electrolyte, $5 \text{ M H}_2\text{SO}_4$, at varied scan rates and at room temperature (20°C). We selected this acid concentration because aqueous solutions of 30 - 50 wt% H_2SO_4 have a freezing point below -20°C , thus allowing us to perform spectroelectrochemistry over a broad temperature range.³⁵ Upon cathodic polarization in acidic electrolytes, tungsten oxides ($\text{WO}_3 \cdot n\text{H}_2\text{O}$ where $n = 0$ or 2) undergo proton-insertion coupled electron transfer (PICET) which leads to an electrochromic response as the initially d^0 metal cation undergoes a 1-electron transfer. This is

described by the following reversible electrochemical reaction in a strongly acidic aqueous electrolyte, where the proton donor is H_3O^+ and x is < 1 :



For an insertion process like PICET, the cyclic voltammogram (CV) response is sensitive to the crystal structure of the insertion host.³⁶ Correspondingly, the room temperature CV of WO_3 (**Figure 2a**) exhibits two pairs of redox peaks at 5 mV/s, labeled 1/1' and 2/2'. We attribute the large current magnitude of peak 2 to the overlap of PICET with the onset of the HER, a competitive proton-coupled electron transfer (PCET) reaction at low potentials. Transmission spectra collected at these redox peaks (**Figure 2b**) indicate broad-spectrum decreased transmission (increased absorption) accompanying peak 1, which is completely reversed at peak 1'. The complete time-dependent transmission data are shown in **Figure 2c**. The onset of coloration above ~ 600 nm is concomitant with peak 1, as shown by the juxtaposition with the current and time traces in the left panel of **2c**. This coloration is reversed at peak 1' returning to the pristine, bleached state.

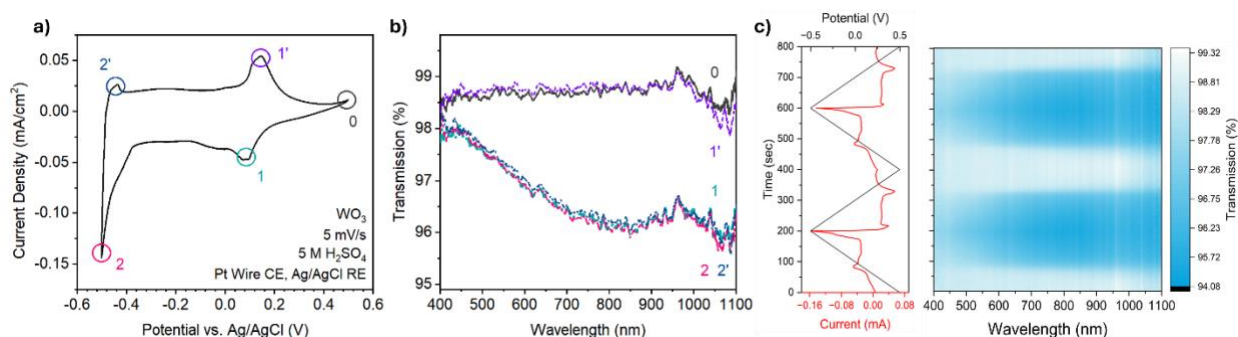


Figure 2. a) CV of WO_3 in 5 M H_2SO_4 at 5 mV/s and 20°C . b) UV/Vis/NIR spectra at selected points during cyclic voltammetry: initial (open circuit, point 0), peak 1, peak 2, peak 2' and peak 1'. c) Color-mapped operando electrochemical UV/Vis/NIR transmission spectra from 400 – 1100 nm. The corresponding CV data is shown in the left panel.

Thin films of $\text{WO}_3 \cdot 2\text{H}_2\text{O}$ were examined under the same conditions as WO_3 . The room temperature CV in 5 M H_2SO_4 at 5 mV/s (**Figure 3a**) exhibits two pairs of redox peaks at 5 mV/s, labeled 3/3' and 4/4'. Individual transmission spectra collected at these peaks (**Figure 3b**) indicate a more gradual decrease in transmission accompanying PICET into $\text{WO}_3 \cdot 2\text{H}_2\text{O}$, as shown by the progression of the transmission spectra from peak 3 to 4. Coloration begins in the NIR region (> 800 nm) and progressively extends to shorter wavelengths at lower reducing potentials. This trend is reversed on the anodic sweep, as shown in the full set of time-dependent transmission spectra in **Figure 3c**. Taken together, this data demonstrates inherent differences in the electrochromic coloration behavior of WO_3 and $\text{WO}_3 \cdot 2\text{H}_2\text{O}$ during reversible PICET. While WO_3 shows a more uniform onset of coloration above 600 nm during the initial stages of PICET, the initial coloration of $\text{WO}_3 \cdot 2\text{H}_2\text{O}$ is restricted to the NIR wavelengths and only gradually extends towards visible wavelengths during reduction. Additionally, the extent of change in the transmission is a near linear gradient from the high-to-low wavelengths in $\text{WO}_3 \cdot 2\text{H}_2\text{O}$, whereas the reduction in transmission is more uniform across wavelengths above 600 nm in WO_3 .

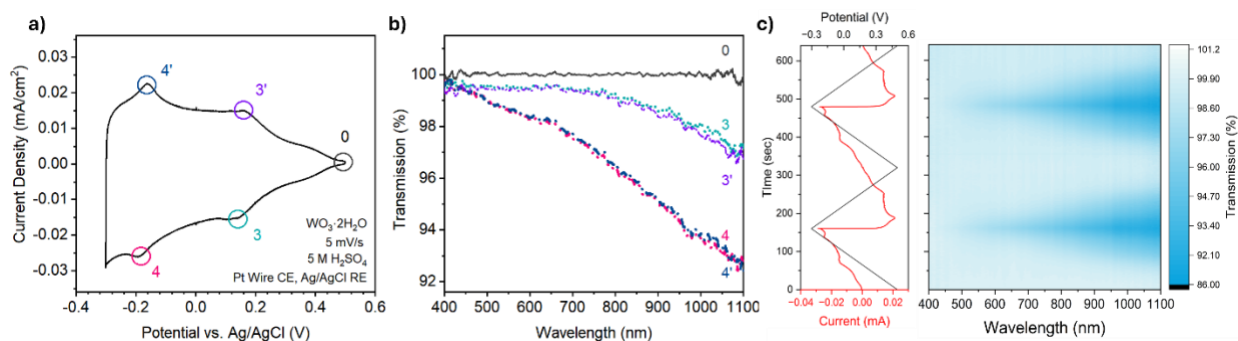


Figure 3. a) Cyclic voltammetry of $\text{WO}_3 \cdot 2\text{H}_2\text{O}$ in 5 M H_2SO_4 at 5 mV/s and 20°C. b) UV/Vis/NIR spectra at selected pointed during cyclic voltammetry: initial (open circuit, point 0), peak 3, peak 4, peak 4', and peak 3'. c) Operando electrochemical UV/Vis/NIR transmission spectra from 400 – 1100 nm. The corresponding CV data is shown in the left panel.

We further examined the electrochromic behavior by differentiating the transmission response of the tungsten oxides with respect to time at specific wavelengths, $\Delta T(\%)/\Delta t(\text{sec})$. By plotting the resulting rate-of-change data against the applied potential, we constructed a spectral analog of a CV. This juxtaposition of voltammetry data with the correlated differential UV/Vis data was utilized previously to characterize electrochromic mechanisms and charge storage processes.^{10,37} We selected two wavelengths for this analysis, 550 nm and 1050 nm, to compare the response in the visible and near-IR regions, respectively. At 20°C, we observe peaks in the WO_3 spectral data which correlate with the first redox couple (1/1') in the CV (**Figure 4a**). The 550 nm peaks occur at lower potentials than the 1050 nm peaks by 50 mV. We also observe that there is little-to-no change in transmission at either wavelength for the low-potential redox couple (2/2'). This may be due to the formation of hydrogen bubbles on the electrode surface from the HER, which could obfuscate the electrochromic response of the underlying film in this transmission-based measurement. The differential transmission of $\text{WO}_3 \cdot 2\text{H}_2\text{O}$ shows coloration at 1050 nm over a broad potential range, with the greatest changes coinciding with redox peaks 3 and 4 (**Figure 4b**). However, at 550 nm, the electrochromic response is decoupled from the CV response, exhibiting a gradual increase in differential transmission as a function of potential. This analysis further emphasizes that while both WO_3 and $\text{WO}_3 \cdot 2\text{H}_2\text{O}$ undergo PICET, their CV and electrochromic response differ substantially.

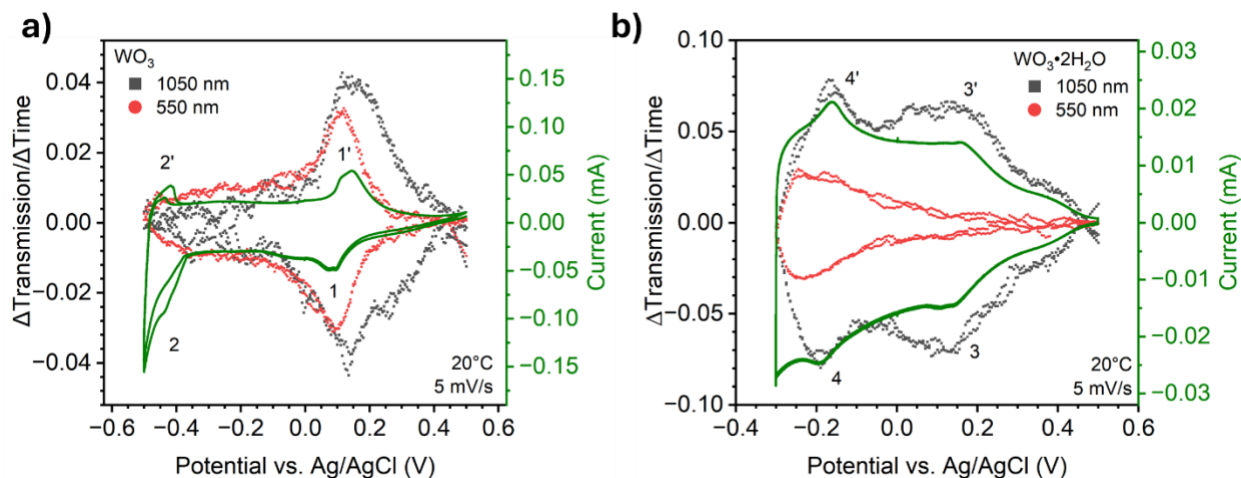


Figure 4. a) Differential transmission during PICET into WO_3 at 550 nm (visible; red dot) and 1050 nm (infrared; black square) as a function of applied potential over two cycles at 5 mV/s and 20°C. The differential transmission data are displayed with the CV (green) to show the relationship between the transmission rate and current response. b) Differential transmission during PICET into $\text{WO}_3 \cdot 2\text{H}_2\text{O}$ for two cycles under the same conditions as for WO_3 in a).

Electronic Structure Considerations

To understand this key difference in the room temperature electrochromic behavior between WO_3 and $\text{WO}_3 \cdot 2\text{H}_2\text{O}$, we considered the differences in their solid-state structures and more specifically the local coordination environment of tungsten (**Figure 5**). In monoclinic WO_3 , W^{6+} is coordinated by six oxygens but they do not form an ideal octahedron: tungsten is displaced from the octahedral center producing three shorter and three longer bonds (**Figure 5**). In the extended structure, these distorted octahedra connect via corners with non-linear W-O-W bond angles, termed octahedral tilting, which has a direct influence on the electronic properties of perovskite-like oxides like WO_3 .³⁸ In monoclinic $\text{WO}_3 \cdot 2\text{H}_2\text{O}$, W^{6+} also resides off the polyhedral center and is coordinated by five oxygens with one water molecule occupying a terminal ligand position (**Figure 5**). The W-OH₂ bond is longer (2.3 Å) than the W-O bonds, which range from 1.7 to 1.9 Å.³⁹ This lengthening of one apical W-OH₂ bond leads to further distortion than in the case

of WO_3 , such that the coordination environment of W^{6+} in $\text{WO}_3 \cdot 2\text{H}_2\text{O}$ approaches that of a square pyramid.

Crystal field theory (CFT) is a simple model that allows us to make predictions about the arrangement of W d-orbitals in different coordination environments. Here we consider increasing octahedral distortion along the continuum between ideal octahedral and ideal square pyramidal coordination (**Figure 5**). Relative to the octahedral case, W d-orbitals with z-components (d_{xz} , d_{yz} , and d_{z^2}) decrease in energy, while orbitals which overlap the x-y plane (d_{xy} and $d_{x^2-y^2}$) increase in energy, resulting in the square pyramidal arrangement of d-orbitals.⁴⁰ We regard the coordination of W in WO_3 to be closer to, but not exactly like, the ideal octahedral coordination, while W approaches square pyramidal coordination in $\text{WO}_3 \cdot 2\text{H}_2\text{O}$. This coordination environment, which we considered from the standpoint of a single octahedron, has a direct influence on the electronic structure of tungsten oxides, since the conduction band is primarily composed of the W d-states, and thus the electrochromic response.

Upon electrochemical PICET, WO_3 undergoes two structural transitions associated with the two redox features observed in the CV. The 1/1' redox couple is associated with the transition between monoclinic WO_3 and a tetragonal hydrogen bronze ($\text{t-H}_x\text{WO}_3$) and the 2/2' redox couple is associated with the transition between $\text{t-H}_x\text{WO}_3$ and a cubic bronze ($\text{c-H}_x\text{WO}_3$).¹⁸ These structural transitions correspond with changes in the pattern of octahedral tilting as well as changes in the local coordination environment of the W-centers, where the W-atom shifts to the centroid of the polyhedral unit and the W-O bond lengths become more similar in length. Extending this CFT analysis to these hydrogen bronze phases, we see that as the degree of PICET increases in WO_3 , the polyhedral units become more similar to a perfect octahedral coordination environment (**Figure 5**). For $\text{WO}_3 \cdot 2\text{H}_2\text{O}$, our previous results indicate that no discrete structural transitions occur during PICET, instead we propose that there may be changes to the degree of octahedral tilting and W-distortion¹⁸, albeit the presence of the axial water molecule inherently distorts the coordination geometry. Though CFT is a simple tool, the prediction of the

relative energy of W d-orbitals is corroborated by the DFT-calculated DOS for WO_3 and $\text{WO}_3 \cdot 2\text{H}_2\text{O}$.

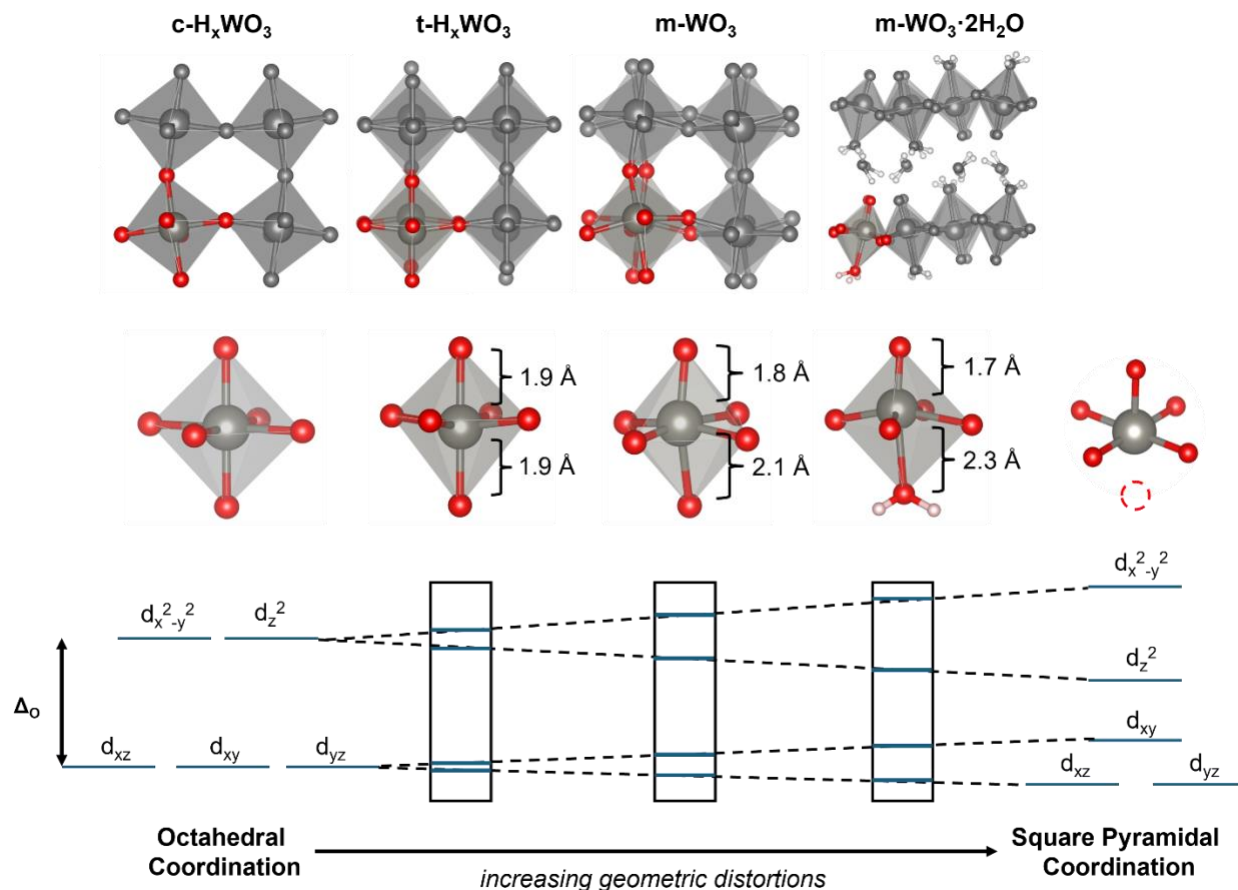


Figure 5. Top: Crystal structures comparison of monoclinic WO_3 with tetragonal (t-) and cubic (c-) H_xWO_3 and monoclinic $\text{WO}_3 \cdot 2\text{H}_2\text{O}$. The repeating octahedral unit is highlighted in color. Middle: Local coordination environment of tungsten in their respective structures. Bottom: d-orbital splitting diagrams based on CFT showing the transition from ideal octahedral to square pyramidal coordination. Tungsten coordination in WO_3 and the H_xWO_3 structures is more like the ideal octahedral case while in $\text{WO}_3 \cdot 2\text{H}_2\text{O}$ it approaches the square pyramidal case.⁴¹

We calculated the DOS of pristine and proton intercalated tungsten oxides ($x = 0.5$) to validate the orbital splitting hypothesis developed with CFT. As expected, DOS results show that

in the pristine oxides (i.e., before PICET), most oxygen states occupy the valence band, while most low-lying conduction band states are composed of W d orbitals (**Figure 6** and **Figures S1 – S2**)²⁵. In $\text{WO}_3 \cdot 2\text{H}_2\text{O}$, we found a narrow energy band centered at approximately 2.9 eV above E_F . This narrow band arises from the d_z^2 orbitals in the model, consistent with the CFT prediction that the d_z^2 orbital decreases in energy due to changes in axial bond lengths. However, our CFT hypothesis could not adequately predict that the d_z^2 orbital would shift to lower energies than the d_{xy} , d_{xz} , and d_{yz} orbitals, as suggested by DFT. This inadequacy results from the differences in the axial bond lengths as well as the different identities and field strengths of the ligands (O^{2-} vs. H_2O) in these axial positions. No such narrow band is observed for WO_3 , where a continuum of low-lying states instead originates from these molecular orbitals (d_{xy} , d_{xz} , and d_{yz}). The DOS calculations on the pristine oxides are therefore consistent with the prediction from CFT and confirm the presence of a narrow conduction band in $\text{WO}_3 \cdot 2\text{H}_2\text{O}$ which we hypothesize is critical to explain its unique electrochromic response.

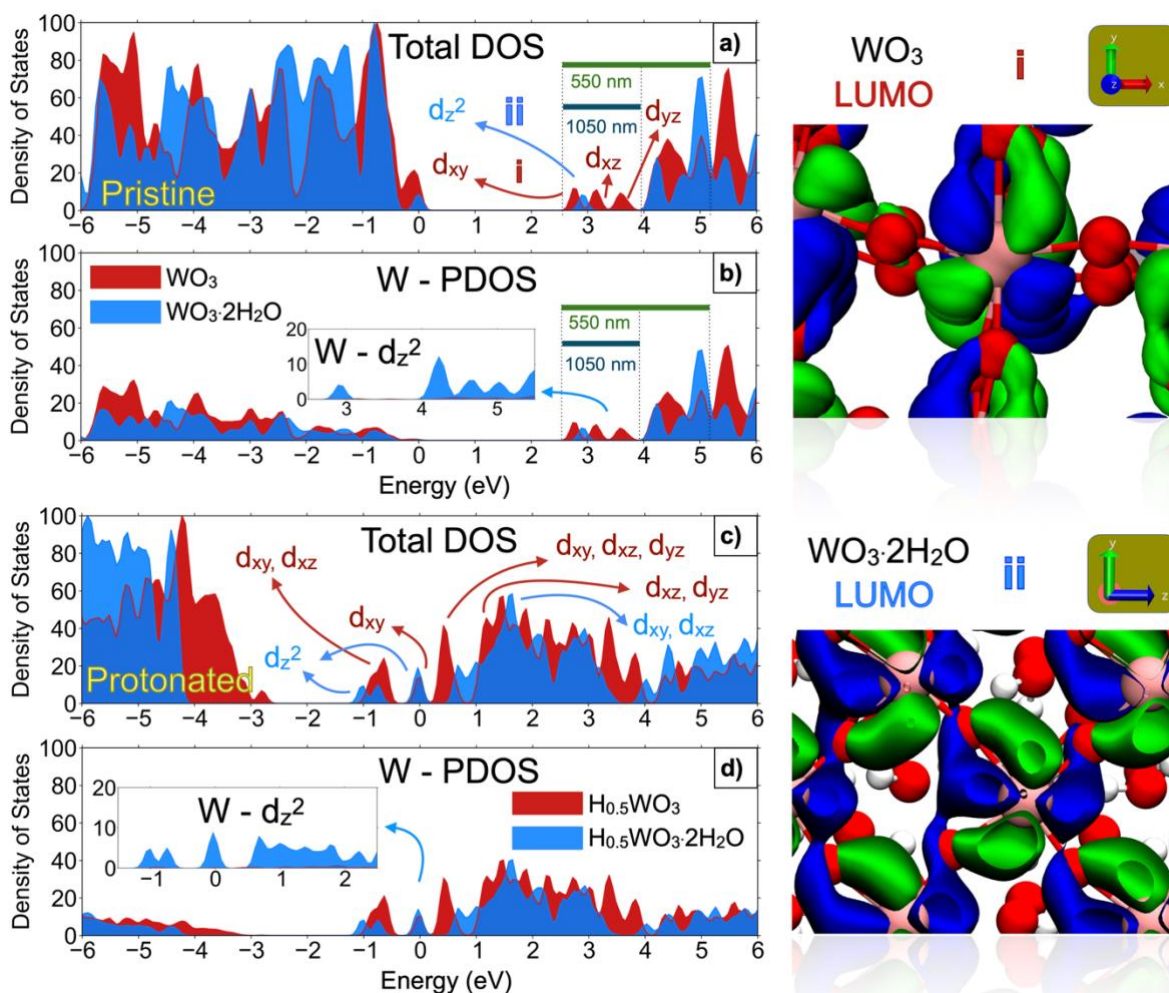


Figure 6. Left panel: DOS profiles for $\text{WO}_3 \cdot n\text{H}_2\text{O}$ and $\text{H}_x\text{WO}_3 \cdot n\text{H}_2\text{O}$ ($n = 0$: red, $n = 2$: cyan, $x = 0.5$): Total (a – pristine, c – protonated), and projected on W atoms (b – pristine, d – protonated). The inset figures on panels (b) and (d) focus on areas of interest and show the DOS projected on the W d_z^2 orbital. DOS profiles are normalized by their respective maximum values. States that considerably contribute to W – d orbitals are shown with colored arrows based on corresponding systems. Right panel: visualization of the LUMO (around W atoms). Blue and green solid surfaces represent opposite phases of the wave function. Orientation vectors in Cartesian space: x – red, y – green, z – blue. Atom color code: W – ochre, O – red, H – white.

Upon PICET to form $\text{H}_{0.5}\text{WO}_3 \cdot 2\text{H}_2\text{O}$, d_z^2 remains the dominant contributor to the LUMO (this LUMO corresponds to $\text{H}_{0.5}\text{WO}_3 \cdot 2\text{H}_2\text{O}$, i.e., after PICET). Furthermore, we observe a similar

behavior of mixed contributions to low-energy peaks from the d_z^2 , d_{xy} , and d_{xz} orbitals in the conduction band of $\text{H}_{0.5}\text{WO}_3 \cdot 2\text{H}_2\text{O}$ in contrast with d_z^2 -dominated contributions in $\text{WO}_3 \cdot 2\text{H}_2\text{O}$ (at ~ 2.9 and 4.3 eV), see **Figure 6**. Contributions to the DOS from different orbitals are summarized in **Figure S3** and **Table S3**.²⁵ Profiles of DOS projected on the specific orbital types are provided in **Figures S4 – S7**.²⁵ In the case of PICET forming $\text{H}_{0.5}\text{WO}_3$, while d_{xy} is the major contributor to the LUMO in WO_3 , there is a comparable contribution from d_{xz} and d_{yz} orbitals to the LUMO of $\text{H}_{0.5}\text{WO}_3$ (**Figure S3**)²⁵ consistent with the CFT predictions for the more symmetric coordination environments of cubic $\text{H}_{0.5}\text{WO}_3$. Consequently, distinct d_{xz} and d_{yz} states at low energies in the conduction band of WO_3 overlapped after PICET contributing to the same DOS peak, i.e., the peak corresponding to the LUMO (at ~ 0.5 eV). Furthermore, mixed contributions from d_{xy} , d_{xz} , d_{yz} orbitals are observed in the rest of the $\text{H}_{0.5}\text{WO}_3$ low-energy DOS peaks in the conduction band.

We evaluated the effect of water on the DOS of WO_3 at various degrees of hydration and states of charge. In this context, DOS is recalculated in the absence of water, i.e., by removing water molecules while keeping the tungstate structure frozen. The two different types of water molecules in $\text{WO}_3 \cdot 2\text{H}_2\text{O}$ are gradually removed. First, H-bonded water molecules are removed, while W-coordinated water molecules remain in the structure, resembling the structure of the monohydrate analogue ($\text{WO}_3 \cdot \text{H}_2\text{O}$). Then, the coordinated water molecules were removed, leaving a vacant ligand site. The resulting DOS profiles are provided in **Figure 7**. We observe the same low-lying d_z^2 energy band in the pristine oxide. This finding suggests that the origin of this effect is geometric in nature. This supports our assumption from the CFT model, where the extension of axial bonds due to bound water approximates a square pyramidal coordination environment. We observe a similar trend upon PICET of $\text{WO}_3 \cdot 2\text{H}_2\text{O}$, i.e., in $\text{H}_{0.5}\text{WO}_3 \cdot 2\text{H}_2\text{O}$.

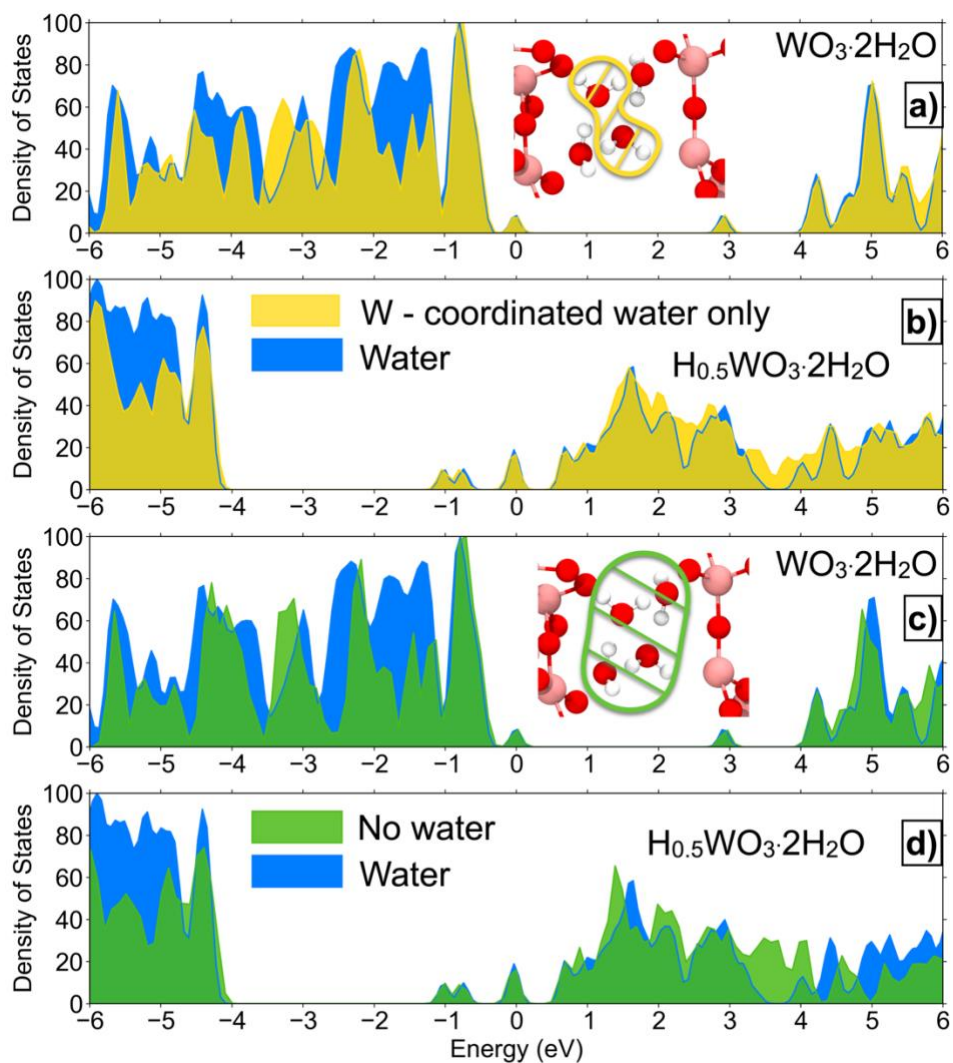


Figure 7. Total DOS of $\text{WO}_3 \cdot 2\text{H}_2\text{O}$. Panels from top to bottom: (a) and (c): $\text{WO}_3 \cdot 2\text{H}_2\text{O}$, (b) and (d): $\text{H}_{0.5}\text{WO}_3 \cdot 2\text{H}_2\text{O}$. Cyan plots: DOS where water is present, yellow plots: DOS where only the W-coordinating water molecules are present (H-bonded water molecules are removed), green plots: DOS where water is completely removed. DOS profiles on each panel are normalized by the maximum value of the DOS where water is present (on the same panel). Examples of different cases of water molecules removed from the $\text{WO}_3 \cdot 2\text{H}_2\text{O}$ are shown as insets in panels (a) and (c).

Based on this theoretical and computational analysis, we consider the impact of the different electronic structures on the electrochromic response during PICET, as electrons populate the conduction band and possibly undergo transitions in energy upon the absorption of optical photons. In WO_3 and $\text{WO}_3 \cdot 2\text{H}_2\text{O}$, tungsten is in the 6^+ oxidation state with a d^0 electron

configuration and thus at room temperature there is minimal occupancy of the outermost W d-orbitals which compose the conduction band. Therefore, both materials are semiconductors with experimentally determined bandgaps of 3.0 and 2.6 eV for WO_3 and $\text{WO}_3 \cdot 2\text{H}_2\text{O}$, respectively.⁴² PICET leads to the formation of $\text{H}_x\text{WO}_3 \cdot n\text{H}_2\text{O}$ (**Equation 2**) and transfer of electrons to the oxide; the state of charge (x) increases as the cathodic potential decreases. We expect electrons to fill the lowest energy conduction band states first (i.e., d_{xy} in WO_3), with the next-lowest energy level available for excitation being the d_{xz} or d_{yz} states. In short, we expect PICET to result in shallow electron doping at the bottom of the conduction band. In WO_3 , electrochromism is associated with optical absorption due to direct transitions of electrons in the conduction band.⁴³ In both oxides, transmittance at 1050 nm decreases even at low states of charge, and its derivative tracks with the CV for all potentials (**Figure 3**). In other words, low energy photons can be absorbed by both oxides at all states of charge ($x > 0$). Transmittance in the visible at 550 nm behaves differently than the NIR response. In WO_3 , it tracks with the CV but at slightly higher states of charge than at 1050 nm. This shift in onset potential for photons of different energies, known as the Moss-Burstein effect, indicates that absorption of higher-energy photons occurs only at higher states of charge or greater electron filling in WO_3 . On the other hand, in $\text{WO}_3 \cdot 2\text{H}_2\text{O}$, the transmittance at 550 nm does not track with the CV except at the highest states of charge. We propose that the larger energy gap between the top and bottom energy levels of the d-orbitals in the conduction band of $\text{WO}_3 \cdot 2\text{H}_2\text{O}$, as predicted by CFT and DFT, is responsible for this wavelength-dependence.

Temperature Dependence

We next consider the influence of temperature between -20 and 20°C on the electrochromic response of tungsten oxides since we expect this to have an impact on the kinetics of PICET as well as competitive PCET reactions like HER. The temperature-dependent CVs for WO_3 at 5 and 100 mV/s are shown in **Figure S10**.²⁵ The overall shape of the CVs is maintained

with temperature although the current slightly decreases leading to a reduction in the capacity with decreasing temperature at both 5 and 100 mV/s. On the other hand, the coulombic efficiency increases as temperature decreases, with a larger improvement at 5 mV/s than 100 mV/s. The largest temperature differences arise in the low potential regions at both scan rates: Peak 2 contains contributions from both PICET and HER, but peak 2' only contains contributions from PICET. We hypothesize that temperature-dependent changes in the low potential region are largely due to suppression of the HER, which explains the trend in coulombic efficiency. The HER ($2\text{H}^+ + 2\text{e}^- \rightarrow \text{H}_2$) requires the transfer of two protons and two electrons, whereas PICET only requires one. As a result, we expect the interfacial kinetics associated with the HER to require higher activation energies than PICET and thus be more sensitive to changes in temperature. The decrease in the HER contribution also leads to an increased current response for peak 2' as temperature decreases, which suggests that some inserted protons could also be participating in the HER, as we proposed in a previous study.¹⁸

The temperature-dependent CVs for $\text{WO}_3 \cdot 2\text{H}_2\text{O}$ at 5 and 100 mV/s also show an overall reduction in current, with a slight decrease in capacity, but overall improvement in the coulombic efficiency at 5 mV/s as temperature decreases (**Figure S11**).²⁵ We also note an observed broadening of the redox peaks as the temperature decreases with peak 3 appearing to nearly disappear completely, though the effect is most notable at 100 mV/s. Unlike for WO_3 , the increase in coulombic efficiency with decreasing temperature is only observed at 5 mV/s. We attribute this difference to the reduced contribution of HER in $\text{WO}_3 \cdot 2\text{H}_2\text{O}$. We previously found that $\text{H}_x\text{WO}_3 \cdot 2\text{H}_2\text{O}$ was a worse HER catalyst than H_xWO_3 , which agrees with these results.¹⁸ A more detailed kinetic analysis of the temperature dependence of the PICET process is discussed in the SI (**Section 5** and **Figure S12**).²⁵ Overall, in both materials we found that PICET is more favored at low temperatures that suppress the parasitic HER.

We performed operando electrochemical UV/Vis/NIR as a function of temperature from -20 to 20°C at 5 and 100 mV/s (**Figure 8** for WO_3 and **9** for $\text{WO}_3 \cdot 2\text{H}_2\text{O}$). We found a gradual

decrease in the background transmission at low temperatures over the timescale of the experiment. We attribute this to the condensation of water on the quartz cuvette from the atmosphere, which was not totally excluded by the Ar gas flowing through the stage. For WO_3 (Figure 8), we observed an increase in coloration for all wavelengths when measured at -10°C and -20°C . As the temperature decreases, transmittance decreases (absorbance increases) while cathodic capacity decreases, leading to an overall improvement in coloration efficiency (the change in optical density per unit charge). This again emphasizes that PICET is more favorable at lower temperatures. For each respective temperature, cycling the WO_3 thin film at 5 mV/s generally yields greater absorbance than cycling at 100 mV/s, though not by a large margin. There is no cycling condition we found for which a sample exhibiting an electrochromic response at 5 mV/s did not also exhibit a similar response at 100 mV/s, which is indicative of both the similar degrees of PICET achieved at both scan rates and the speed of the electrochromic response.

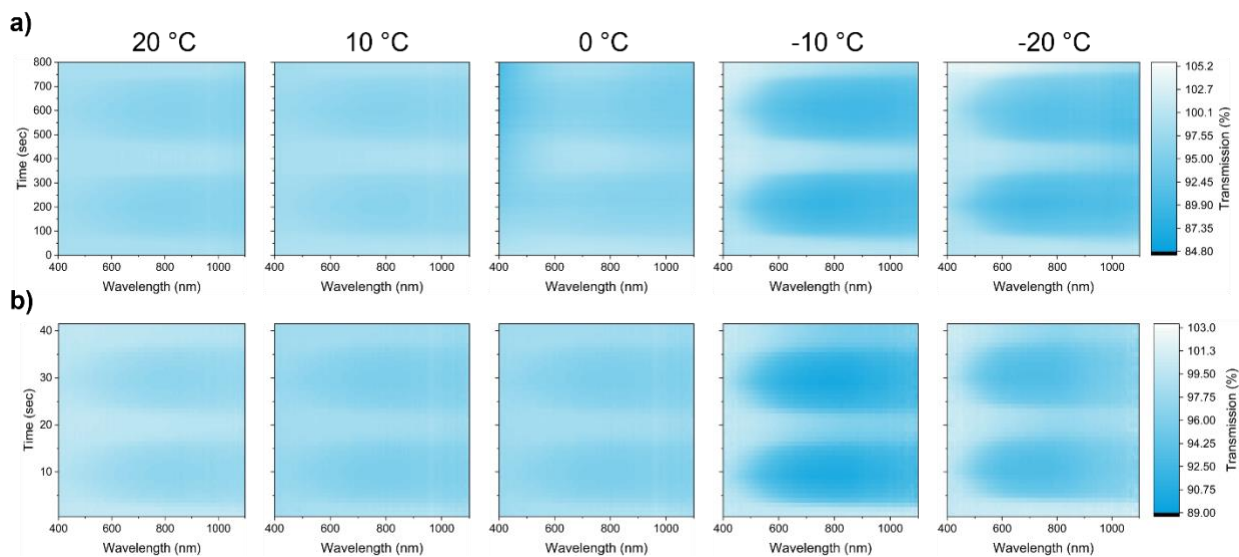


Figure 8. Temperature dependent operando electrochemical UV/Vis/NIR spectroscopy of WO_3 for two cycles for each temperature at a) 5 mV/s and b) 100 mV/s.

In $\text{WO}_3 \cdot 2\text{H}_2\text{O}$, at both 5 mV/s and 100 mV/s the film achieves similar degrees of reduction in transmission (**Figure 9**) and demonstrates the same general triangular shape in the operando UV/Vis/NIR response. Unlike WO_3 , $\text{WO}_3 \cdot 2\text{H}_2\text{O}$ does not exhibit an increase in coloration at decreased temperatures, perhaps due to its smaller overall degree of PICET. Rather, the operando spectra at -10 and -20°C become partially obscured by the aforementioned changes in background spectra due to water condensation within the sample stage.

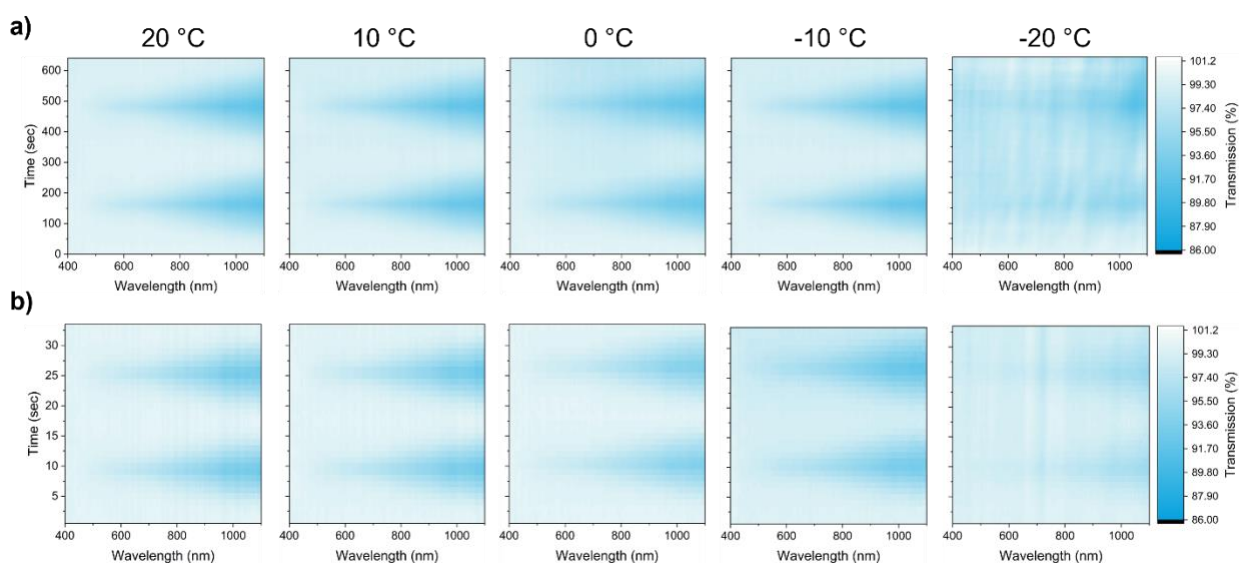


Figure 9. Operando UV/Vis/NIR spectroscopy results shown over two cycles for each temperature at a) 5 mV/s and b) 100 mV/s.

4. Conclusions

In this study, we analyzed the electrochromic response of WO_3 and $\text{WO}_3 \cdot 2\text{H}_2\text{O}$ thin films in 5 M H_2SO_4 electrolyte. Differentiating the operando UV/Vis/NIR response shows that the visible wavelength response in $\text{WO}_3 \cdot 2\text{H}_2\text{O}$ is strongly potential dependent, where the near-IR response is more strongly correlated with the degree of PICET. The correlation between the current response and the degree of coloration is also observed for both the visible and near-IR in WO_3 . We present our hypothesis based on the d-orbital splitting predicted by CFT, with the increased

degree of splitting for $\text{WO}_3 \cdot 2\text{H}_2\text{O}$ resulting in a larger intra-band transition from the lowest energy d_z^2 orbital to the higher energy d_{xy} and d_{xz} orbitals. This hypothesis is corroborated by DOS calculations for $\text{H}_x\text{WO}_3 \cdot n\text{H}_2\text{O}$ ($n = 0$ or 2 , $x = 0.0$ or 0.5). These calculations demonstrate that the formation of a ~ 2.9 eV d_z^2 band arising from the axial bond length distortions in $\text{WO}_3 \cdot 2\text{H}_2\text{O}$ results in divergence of the visible and near-infrared absorption conditions. This divergence may in turn drive the dual-band response for $\text{WO}_3 \cdot 2\text{H}_2\text{O}$ which is not observed in WO_3 . Hydration affects the largest contribution to the low-energy states in the conduction band (less than 4 eV above E_F) that are composed of d_{xy} , d_{xz} , and d_{yz} in WO_3 and solely d_z^2 in $\text{WO}_3 \cdot 2\text{H}_2\text{O}$. By gradually removing water molecules from $\text{WO}_3 \cdot 2\text{H}_2\text{O}$ and keeping the tungsten oxide (W-O) structure intact, we observed that the low-energy conduction band orbitals are practically unaffected by the presence of water. Consequently, we postulate that the conduction band changes between H_xWO_3 and $\text{H}_x\text{WO}_3 \cdot 2\text{H}_2\text{O}$ ($x = 0.0, 0.5$) are due to changes in the crystal structure upon hydration. The temperature-dependent UV/Vis/NIR response revealed an increase in raw absorbance as well as coloration efficiency for WO_3 which was not observed for $\text{WO}_3 \cdot 2\text{H}_2\text{O}$. We hypothesize that the suppression of the HER at low temperatures increases the degree of PICET and thus the coloration efficiency of WO_3 . Overall, this work shows how the local coordination of tungsten in tungsten oxide films can be utilized to tune the electronic structure and modify the electrochromic properties.

5. Acknowledgements

We acknowledge the contributions of Prof. Lena Kourkoutis towards useful discussions on low temperature structural transitions and cryo-TEM of tungsten oxides, to whom we dedicate this manuscript. We thank Prof. Delia Milliron, Prof. Wennie Wang, and Dr. Saeed Saeed for useful discussions on the electrochromic response of tungsten oxides. Tungsten oxide synthesis and UV-VIS-NIR spectroelectrochemistry were supported by the U.S. National Science Foundation under grant DMR-1653827. This work made use of the electron microscopy facility of

the Platform for the Accelerated Realization, Analysis, and Discovery of Interface Materials (PARADIM), which is supported by the National Science Foundation under Cooperative Agreement No. DMR-2039380. LK and GM acknowledge support from the U.S. Department of Energy, Office of Science, Office of Basic Energy Sciences under Award No. DE-SC0023465 for DFT calculations. This report was prepared as an account of work sponsored by an agency of the United States Government. Neither the United States Government nor any agency thereof, nor any of their employees, makes any warranty, express or implied, or assumes any legal liability or responsibility for the accuracy, completeness, or usefulness of any information, apparatus, product, or process disclosed, or represents that its use would not infringe privately owned rights. Reference herein to any specific commercial product, process, or service by trade name, trademark, manufacturer, or otherwise does not necessarily constitute or imply its endorsement, recommendation, or favoring by the United States Government or any agency thereof. The views and opinions of authors expressed herein do not necessarily state or reflect those of the United States Government or any agency thereof. This research was supported in part by the University of Pittsburgh Center for Research Computing and Data, RRID:SCR_022735, through the resources provided. Specifically, this work used the H2P cluster, which is supported by NSF award number OAC-2117681. In addition, this work was supported by computational time granted from the National Infrastructures for Research and Technology S.A. (GRNET S.A.) in the National HPC facility - ARIS - under project ID pr017025. OpenAI ChatGPT-40 was used for refining the manuscript text. The tool was used in a manner that does not conflict with APS ethical policies and the authors take full responsibility for the content.

6. References

- (1) Gu, C.; Jia, A. B.; Zhang, Y. M.; Zhang, S. X. A. Emerging Electrochromic Materials and Devices for Future Displays. *Chem. Rev.* **2022**, *122* (18), 14679–14721.
<https://doi.org/10.1021/acs.chemrev.1c01055>.

- (2) Fu, G.; Gong, H.; Xu, J.; Zhuang, B.; Rong, B.; Zhang, Q.; Chen, X.; Liu, J.; Wang, H. Highly Integrated All-in-One Electrochromic Fabrics Camouflage. *J. Mater. Chem. A* **2024**, *12*, 6351–6358. <https://doi.org/10.1039/d3ta07562a>.
- (3) Wu, S.; Sun, H.; Duan, M.; Mao, H.; Wu, Y.; Zhao, H.; Lin, B. Applications of Thermochromic and Electrochromic Smart Windows: Materials to Buildings. *Cell Reports Phys. Sci.* **2023**, *4* (5), 101370. <https://doi.org/10.1016/j.xcrp.2023.101370>.
- (4) Niklasson, G. A.; Granqvist, C. G. Electrochromics for Smart Windows : Thin Films of Tungsten Oxide and Nickel Oxide, and Devices Based on These. *J. Mater. Chem.* **2007**, *17*, 127–156. <https://doi.org/10.1039/b612174h>.
- (5) Granqvist, C. Electrochromic Metal Oxides: An Introduction to Materials and Devices. In *Electrochromic Materials and Devices*; Mortimer, R. J., Rosseinsky, D. R., Monk, P. M. S., Eds.; WILEY-VCH, 2013; pp 3–33.
- (6) Deb, S. K. Optical and Photoelectric Properties and Colour Centres in Thin Films of Tungsten Oxide. *Philos. Mag.* **1973**, *27* (4), 801–822. <https://doi.org/10.1080/14786437308227562>.
- (7) Granqvist, C. G. Electrochromic Materials: Microstructure, Electronic Bands, and Optical Properties. *Appl. Phys. A Solids Surfaces* **1993**, *57* (1), 3–12. <https://doi.org/10.1007/BF00331209>.
- (8) Judeinstein, P.; Livage, J. Role of the Water Content on the Electrochromic Properties of $\text{WO}_3 \cdot n\text{H}_2\text{O}$ Thin Films. *Mater. Sci. Eng. B* **1989**, *3* (1–2), 129–132. [https://doi.org/10.1016/0921-5107\(89\)90191-8](https://doi.org/10.1016/0921-5107(89)90191-8).
- (9) Besnardiere, J.; Ma, B.; Torres-Pardo, A.; Wallez, G.; Kabbour, H.; González-Calbet, J. M.; Von Bardeleben, H. J.; Fleury, B.; Buissette, V.; Sanchez, C.; Le Mercier, T.; Cassaignon, S.; Portehault, D. Structure and Electrochromism of Two-Dimensional Octahedral Molecular Sieve h' - WO_3 . *Nat. Commun.* **2019**, *10* (1), 1–9. <https://doi.org/10.1038/s41467-018-07774-x>.

- (10) Fortunato, J.; Zydlewski, B. Z.; Lei, M.; Holzapfel, N. P.; Chagnot, M.; Mitchell, J. B.; Lu, H. C.; Jiang, D. E.; Milliron, D. J.; Augustyn, V. Dual-Band Electrochromism in Hydrated Tungsten Oxide. *ACS Photonics* **2023**, *10* (9), 3409–3418.
<https://doi.org/10.1021/acsp Photonics.3c00921>.
- (11) Laurinavichute, V. K.; Yu.vassiliev, S.; Khokhlov, A. A.; Plyasova, L. M.; Molina, I. Y.; Tsirlina, G. A. Electrodeposited Oxotungstate Films: Towards the Molecular Nature of Recharging Processes. *Electrochim. Acta* **2011**, *56* (10), 3530–3536.
<https://doi.org/10.1016/j.electacta.2010.10.077>.
- (12) Kühne, T. D.; Iannuzzi, M.; Del Ben, M.; Rybkin, V. V.; Seewald, P.; Stein, F.; Laino, T.; Khaliullin, R. Z.; Schütt, O.; Schiffmann, F.; Golze, D.; Wilhelm, J.; Chulkov, S.; Bani-Hashemian, M. H.; Weber, V.; Borštnik, U.; Taillefumier, M.; Jakobovits, A. S.; Lazzaro, A.; Pabst, H.; Müller, T.; Schade, R.; Guidon, M.; Andermatt, S.; Holmberg, N.; Schenter, G. K.; Hehn, A.; Bussy, A.; Belleflamme, F.; Tabacchi, G.; Glöß, A.; Lass, M.; Bethune, I.; Mundy, C. J.; Plessl, C.; Watkins, M.; VandeVondele, J.; Krack, M.; Hutter, J. CP2K: An Electronic Structure and Molecular Dynamics Software Package -Quickstep: Efficient and Accurate Electronic Structure Calculations. *J. Chem. Phys.* **2020**, *152* (19), 194103.
<https://doi.org/10.1063/5.0007045>.
- (13) Lee, Y.; Lee, T.; Jang, W.; Soon, A. Unraveling the Intercalation Chemistry of Hexagonal Tungsten Bronze and Its Optical Responses. *Chem. Mater.* **2016**, *28* (13), 4528–4535.
<https://doi.org/10.1021/acs.chemmater.5b03980>.
- (14) Hinuma, Y.; Hayashi, H.; Kumagai, Y.; Tanaka, I.; Oba, F. Comparison of Approximations in Density Functional Theory Calculations : Energetics and Structure of Binary Oxides. *Phys. Rev. B* **2017**, *094102* (96), 1–24. <https://doi.org/10.1103/PhysRevB.96.094102>.
- (15) Heyd, J.; Scuseria, G. E.; Ernzerhof, M. Hybrid Functionals Based on a Screened Coulomb Potential. *J. Chem. Phys.* **2003**, *118* (18), 8207–8215.
<https://doi.org/10.1063/1.1564060>.

- (16) Gomes, R.; de Sousa Pinheiro, G.; Serra, E. C.; Moreira, E.; Braga, S. D.; Azevedo, D. L.; Luz Lima, C. da. Theoretical and Experimental Study of the Optoelectronic, Thermodynamic and Vibrational Properties of the Nanostructure of m-WO₃. *Ceram. Int.* **2024**, *50* (5), 8141–8149. <https://doi.org/10.1016/j.ceramint.2023.12.144>.
- (17) Zhu, F.; Ma, C.; Gu, L.; Chen, G.; Zhang, J.; Cong, S.; Zhao, Z.; Zhang, X. Off-Centered-Symmetry-Based Band Structure Modulation of Hexagonal WO₃. *J. Phys. Condens. Matter* **2019**, *31* (35), 355501. <https://doi.org/10.1088/1361-648X/ab2327>.
- (18) Spencer, M. A.; Holzapfel, N. P.; You, K. E.; Mpourmpakis, G.; Augustyn, V. Participation of Electrochemically Inserted Protons in the Hydrogen Evolution Reaction on Tungsten Oxides. *Chem. Sci.* **2024**, *15* (14), 5385–5402. <https://doi.org/10.1039/d4sc00102h>.
- (19) Perdew, J. P.; Yang, W.; Burke, K.; Yang, Z.; Gross, E. K. U.; Scheffler, M.; Scuseria, G. E.; Henderson, T. M.; Zhang, I. Y.; Ruzsinszky, A.; Peng, H.; Sun, J.; Trushin, E.; Görling, A. Understanding Band Gaps of Solids in Generalized Kohn-Sham Theory. *Proc. Natl. Acad. Sci. U. S. A.* **2017**, *114* (11), 2801–2806. <https://doi.org/10.1073/pnas.1621352114>.
- (20) Hartwigsen, C.; Goedecker, S.; Hutter, J. Relativistic Separable Dual-Space Gaussian Pseudopotentials from H to Rn. *Phys. Rev. B* **1998**, *58* (7), 3641–3662.
- (21) Goedecker, S.; Teter, M.; Hutter, J. Separable Dual-Space Gaussian Pseudopotentials. *Phys. Rev. B* **1996**, *54* (3), 1703–1710.
- (22) Vandevondele, J.; Krack, M.; Mohamed, F.; Parrinello, M.; Chassaing, T.; Hutter, J. Quickstep: Fast and Accurate Density Functional Calculations Using a Mixed Gaussian and Plane Waves Approach. *Comput. Phys. Commun.* **2005**, *167* (2), 103–128. <https://doi.org/10.1016/j.cpc.2004.12.014>.
- (23) Guidon, M.; Hutter, J.; Vandevondele, J. Auxiliary Density Matrix Methods for Hartree-Fock Exchange Calculations. *J. Chem. Theory Comput.* **2010**, *6* (8), 2348–2364. <https://doi.org/10.1021/ct1002225>.

- (24) Data from This Work Is Openly Available at <https://doi.org/10.5281/Zenodo.15991318>.
- (25) See Supplemental Material at <https://doi.org/10.1103/Ldg7-Vms5> for Further Description, Tables S1-S4, and Figures S1-S12. The SM Includes Computational Details, Physical and Electrochemical Characterization and Analysis, as Well as Additional Refs. 26-31.
- (26) Perdew, J. P.; Burke, K.; Ernzerhof, M. Generalized Gradient Approximation Made Simple. *Phys. Rev. Lett.* **1996**, *77* (18), 3865–3868.
<https://doi.org/10.1103/PhysRevLett.77.3865>.
- (27) Grimme, S.; Antony, J.; Ehrlich, S.; Krieg, H. A Consistent and Accurate Ab Initio Parametrization of Density Functional Dispersion Correction (DFT-D) for the 94 Elements H-Pu. *J. Chem. Phys.* **2010**, *132* (15). <https://doi.org/10.1063/1.3382344>.
- (28) VandeVondele, J.; Hutter, J. Gaussian Basis Sets for Accurate Calculations on Molecular Systems in Gas and Condensed Phases. *J. Chem. Phys.* **2007**, *127* (11).
<https://doi.org/10.1063/1.2770708>.
- (29) Head, J. D.; Zerner, M. C. A Broyden-Fletcher-Goldfarb-Shanno Optimization Procedure for Molecular Geometries. *Chem. Phys. Lett.* **1985**, *122* (3), 264–270.
[https://doi.org/10.1016/0009-2614\(85\)80574-1](https://doi.org/10.1016/0009-2614(85)80574-1).
- (30) Agmon, N. The Grotthuss Mechanism. *Chem. Phys. Lett.* **1995**, *50* (October), 456–462.
- (31) Wang, M.; He, Y.; Da, M.; Rougier, A.; Diao, X. Temperature Dependence of the Electrochromic Properties of Complementary NiO // WO₃ Based Devices. *Sol. Energy Mater. Sol. Cells* **2021**, *230* (April), 111239. <https://doi.org/10.1016/j.solmat.2021.111239>.
- (32) Freedman, M. L. The Tungstic Acids. *J. Am. Chem. Soc.* **1959**, *81* (15), 3834–3839.
<https://doi.org/10.1021/ja01524a009>.
- (33) Runnerstrom, E. L.; Llordés, A.; Lounis, S. D.; Milliron, D. J. Nanostructured Electrochromic Smart Windows: Traditional Materials and NIR-Selective Plasmonic Nanocrystals. *Chem. Commun.* **2014**, *50* (74), 10555–10572.

- <https://doi.org/10.1039/c4cc03109a>.
- (34) Evans, R. C.; Austin, R.; Miller, R. C.; Preston, A.; Nilsson, Z. N.; Ma, K.; Sambur, J. B. Surface-Facet-Dependent Electrochromic Properties of WO₃ Nanorod Thin Films: Implications for Smart Windows. *ACS Appl. Nano Mater.* **2021**, *4* (4), 3750–3759. <https://doi.org/10.1021/acsnm.1c00215>.
- (35) Ohtake, T. Freezing Points of H₂SO₄ Aqueous Solutions and Formation of Stratospheric Ice Clouds. *Tellus* **1992**, *45B*, 138–144.
- (36) Holzapfel, N. P.; Augustyn, V.; Balland, V. Fundamentals of Proton-Insertion Coupled Electron Transfer (PICET) in Metal Oxides for Aqueous Batteries. *ACS Energy Lett.* **2025**, *10*, 1143–1164. <https://doi.org/10.1021/acseenergylett.4c03076>.
- (37) Zhang, D.; Wang, R. (John); Wang, X.; Gogotsi, Y. In Situ Monitoring Redox Processes in Energy Storage Using UV–Vis Spectroscopy. *Nat. Energy* **2023**, *8* (6), 567–576. <https://doi.org/10.1038/s41560-023-01240-9>.
- (38) Eng, H. W.; Barnes, P. W.; Auer, B. M.; Woodward, P. M. Investigations of the Electronic Structure of D0 Transition Metal Oxides Belonging to the Perovskite Family. *J. Solid State Chem.* **2003**, *175* (1), 94–109. [https://doi.org/10.1016/S0022-4596\(03\)00289-5](https://doi.org/10.1016/S0022-4596(03)00289-5).
- (39) Daniel, M. F.; Desbat, B.; Lassegues, J. C.; Gerand, B.; Figlarz, M. Infrared and Raman Study of WO₃ Tungsten Trioxides and WO₃xH₂O Tungsten Trioxide Hydrates. *J. Solid State Chem.* **1987**, *67* (2), 235–247. [https://doi.org/10.1016/0022-4596\(87\)90359-8](https://doi.org/10.1016/0022-4596(87)90359-8).
- (40) Weber, B. Bond Theories. In *Coordination Chemistry: Basics and Current Trends*; Springer-Verlag: Heidelberg, Germany, 2023; pp 47–72.
- (41) Dunn, T. M. *Some Aspects of Crystal Field Theory*, First.; Harper & Row: New York, 1965.
- (42) Holzapfel, N. P.; Chagnot, M.; Abdar, P. S.; Paudel, J. R.; Crumlin, E. J.; Mckone, J. R.; Augustyn, V. Solution-Phase Synthesis of Platinum-Decorated Hydrogen Tungsten Bronzes for Hydrogen Atom Transfer from Oxides to Molecules. *Chem. Mater.* **2024**, *36*,

11684–11696. <https://doi.org/10.1021/acs.chemmater.4c02814>.

- (43) Wang, W.; Peelaers, H.; Shen, J. X.; Van De Walle, C. G. Carrier-Induced Absorption as a Mechanism for Electrochromism in Tungsten Trioxide. *MRS Commun.* **2018**, *8* (3), 926–931. <https://doi.org/10.1557/mrc.2018.115>.